Turkish Journal of Electrical Engineering & Computer Sciences

http://journals.tubitak.gov.tr/elektrik/

Research Article

Turk J Elec Eng & Comp Sci
(2018) 26: 1453 – 1469

doi:10.3906/elk-1703-366

Experimental realization of a multi-input buck–boost DC–DC converter

Kushal KANHAV[1,*], **Madhuri CHAUDHARI**[2]

[1]Department of Electrical Engineering, St. Vincent Pallotti College of Engineering and Technology, RTM Nagpur University, Nagpur, India

[2]Department of Electrical Engineering, Visvesvaraya National Institute of Technology, Nagpur, India

Received: 31.03.2017 • **Accepted/Published Online:** 12.11.2017 • **Final Version:** 30.05.2018

Abstract: In this paper, steady and dynamic performance of a multi-input buck–boost DC–DC converter is presented. The converter has the ability to supply energy from storage and renewable energy sources individually to the load. It maintains a constant output voltage under various transient conditions of load as well as source. It has the capability to operate in buck, boost, and buck–boost modes of operation. The mathematical model of the converter is developed, which is further used to design controllers for the converter. A laboratory prototype is developed for experimental realization of the converter. The analysis, design, simulation, and experimental results of the converter prove that it is suitable in hybrid electric or renewable energy systems application.

Key words: Multi-input converter, buck–boost, DC–DC converter

1. Introduction

Limited supply of fossil fuels and conventional energy sources has encouraged the development of renewable and hybrid energy systems (RESs and HESs, respectively). HESs can meet future energy demands; hence they are becoming increasingly popular in the area of electrical power systems. Multi-input converter (MIC) systems are becoming more common than multiple single-input DC–DC converters in many applications due to their advantages in terms of size, volume, flexibility in control, reliability, cost efficiency, and voltage regulation [1–8]. Different MIC topologies proposed by the research community mainly focus on nonisolated and isolated structures [9–13]. Isolated structures are bulky, complex, and costly as a transformer is essential for their construction. Nonisolated structures do not use transformers; hence they are simple, economical, and compact. Different approaches to synthesize MICs are reported in [4,14]. The control of MIC topologies for unified power management is presented in [15]. In electric vehicles, ultracapacitors (UCs) are utilized in conjunction with battery packs to increase the peak power rating of the vehicle while maintaining the battery's rating near the average requirement [16]. A hybrid system with renewable energy sources using a buck converter is designed for energy storage topology such as battery or fuel cell, whose performance for various load settings is presented in [17]. Different control strategies and converter topologies are proposed to optimize switching losses, thereby increasing the efficiency of the converter [18–20]. Basic DC–DC converter topology has encouraged the development of majority of MIC topologies. However, they are not fully explored and synthesized, which gives scope for modifications and improvements in their topological structures.

In this paper, a multi-input buck–boost converter (MIBBC) with asymmetrical input sources is analyzed

*Correspondence: kushal.kanhav@gmail.com

and the operation of the MIBBC in buck, boost, and buck–boost mode is verified experimentally. Small-signal analysis of the MIBBC considering nonidealities is presented in detail, which is used to derive various transfer functions of the MIBBC. A comparison of the MIBBC with the existing work is also discussed. The MIBBC has less part counts and its performance is satisfactory for different operating conditions. The input sources and the load are isolated throughout the operation of the MIBBC without using a transformer. The continuity in power supply to the load is maintained with desired output voltage during sudden disconnection of one of the main sources, which proves the reliability of the MIBBC. The control of the MIBBC is simple for all operating conditions. The operation of the MIBBC in buck, boost, and buck–boost mode with less part count makes it suitable in RES and HES applications. Thus, it has the advantage in terms of cost, mass, complexity, and size.

This paper is divided into sections as follows: circuit operation, mathematical analysis and modeling are presented in Section 2. The control strategy of the MIBBC is discussed in Section 3. Results and discussions are presented in section 4. The paper is concluded in Section 5.

2. Analysis of MIBBC

The MIBBC consists of two input sources, V_1 and V_2, connected to a supply load. The load voltage and current (V_o, i_o), inductor voltage (V_L), inductor current (i_L), capacitor current (i_c), and currents (i_1, i_2 and i_3) are represented in Figure 1.

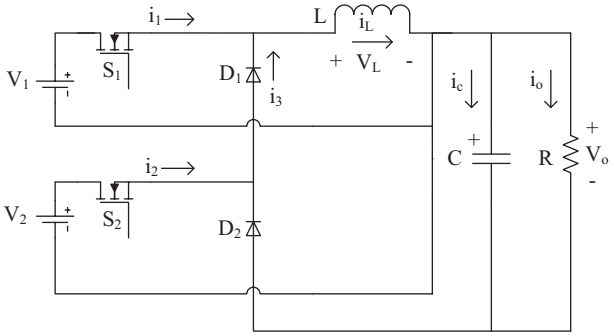

Figure 1. Circuit diagram of the MIBBC.

2.1. Steady state analysis

Operating states of the MIBBC are decided by conduction of switches and power supplied by the sources to the load. Figure 2a shows all possible operating states of the MIBBC, which are summarized in Table 1.

Table 1. Operating states of MIBBC ($V_1 > V_2$).

States	Active source	Switch ON state	V_L	L status	i_3	i_o
1	V_1	S_1	V_1	charging	0	$-i_c$
2	V_2	S_2	V_2	charging	i_2	$-i_c$
3	None	D_1, D_2	$-V_o$	discharging	i_L	$i_L - i_c$

Duty cycles of switches are S_1, S_2 are d_1 and d_2 respectively. The time period (T_S) for one complete switching cycle of gate pulse is shown in Figure 2b. The ideal waveforms of inductor voltage (V_L), inductor current (i_L), and capacitor current (i_c) for all operating states of the MIBBC over a single switching period are shown in Figure 2c. The levels and characteristics of sources V_1 and V_2 may be distinct; hence, during

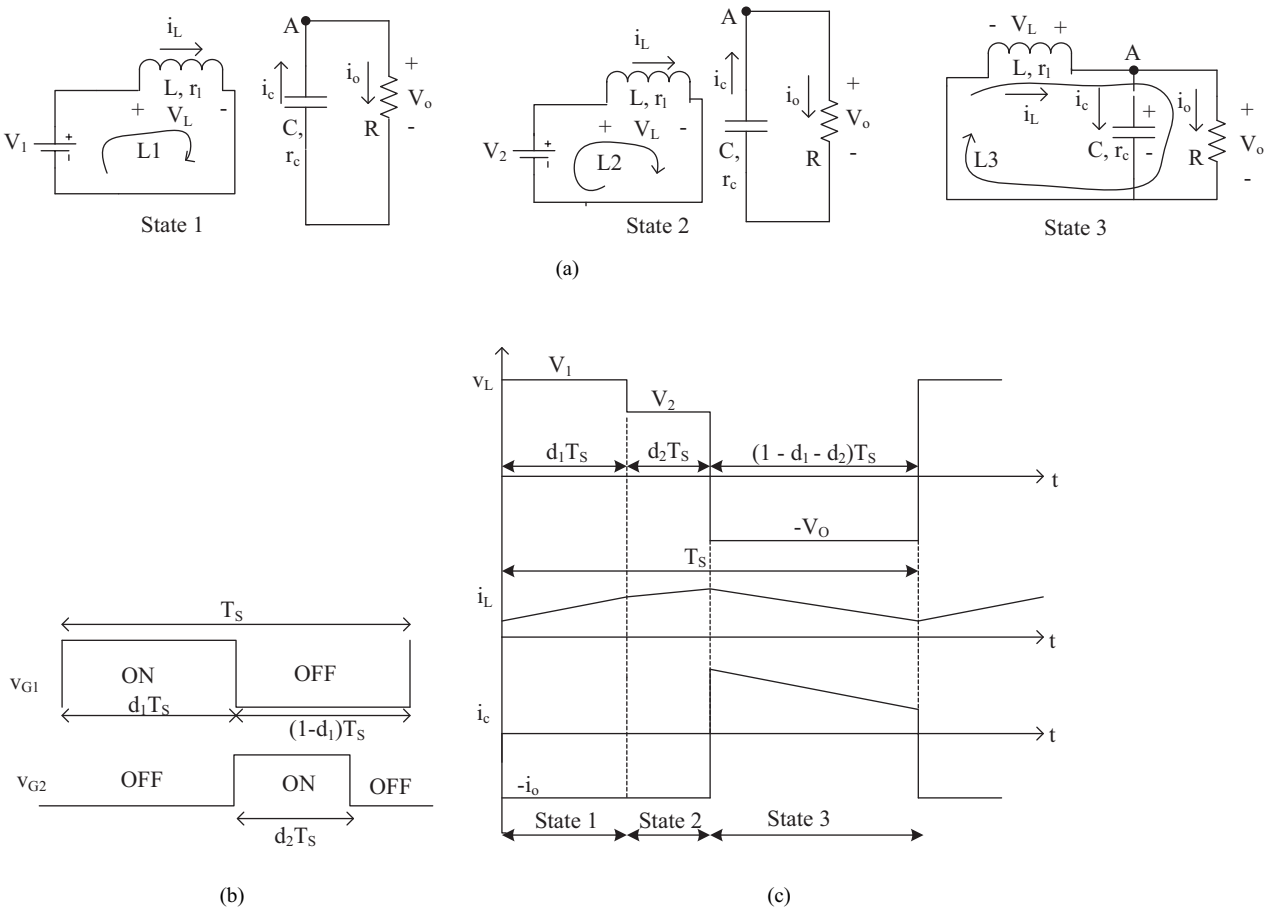

Figure 2. Equivalent circuits and ideal waveforms of the MIBBC (a) operating states, (b) gate signals, and (c) inductor voltage and current, capacitor current.

the operation of MIBBC, simultaneous conduction of S_1 and S_2 is avoided. The losses due to switching and resistive drop across passive elements are neglected. The analysis of the MIBBC in steady state for CCM is as follows: the average value of V_L in one switching cycle is zero according to volt-second balance theory [21]. From Figure 2c, time durations of the MIBBC operating states in terms of duty ratio are given below.

$$\left.\begin{aligned} t_1&=d_1T_s \\ t_2&=d_2T_s \\ t_3&=(1-d_1-d_2)T_s \\ T_s&=t_1+t_2+t_3 \end{aligned}\right\} \tag{1}$$

$$\text{Average inductor voltage } = \int_0^{Ts} V_L dt = 0 \tag{2}$$

$$\text{Therefore, } V_o=V_c=\frac{v_1 d_1}{(1-d_1-d_2)}+\frac{v_2 d_2}{(1-d_1-d_2)} \tag{3}$$

C $\frac{dV_o}{dt}\big|_{T_s} = i_c$ and from state 3,

$$i_c{=}i_L - i_o{=}i_L - \frac{V_o}{R}, \tag{4}$$

where R is the load resistance.

For lossless system, input power (P_i) = output power (P_o). Thus,

$$V_1I_1{+}V_2I_2{=}V_o{\times}I_o, \tag{5}$$

where R is the average value of load current. Therefore,

$$I_o{=}\frac{V_1I_1 + V_2I_2}{V_1d_1 + V_2d_2}{\times}(1{-}d_1{-}d_2) \tag{6}$$

$$I_1{=}d_1I_L \text{ and } I_2{=}d_2I_L, \tag{7}$$

where I_1, I_2, and I_L are average values of source and inductor current, respectively.

$$I_1{=}\frac{d_1I_o}{(1{-}d_1{-}d_2)},\ I_2{=}\frac{d_2I_o}{(1{-}d_1{-}d_2)};\ \text{therefore, } I_L{=}\frac{I_o}{(1{-}d_1{-}d_2)} \tag{8}$$

From Eq. (8)

$$\frac{I_1}{I_2}{=}\frac{d_1}{d_2} \tag{9}$$

Inductor current ripple (Δi_L) and output voltage ripple (Δv_c) give the values of L and C, which are calculated using the following expressions:

$$\Delta i_L{=}\frac{V_o(1 - d_1 - d_2)}{Lf_s} \text{ and } \Delta v_c{=}\frac{V_o(d_1 + d_2)}{RCf_s} \tag{10}$$

The average value of output voltage, considering the nonidealities of the circuit elements, is obtained as follows:

The circuit equations for States 1, 2, and 3 are obtained by applying KVL in loops L_1, L_2, L_3, and KCL at node A, as shown in Figure 2a, as follows:

$$State1 : r_li_L{+}L\frac{di_L}{dt}{=}V_1 \tag{11}$$

$$C\frac{dv_c}{dt}{+}\frac{V_o}{R}{=}0 \tag{12}$$

$$State2 : r_li_L{+}L\frac{di_L}{dt}{=}V_2 \tag{13}$$

$$C\frac{dv_c}{dt}{+}\frac{V_o}{R}{=}0 \tag{14}$$

$$State3 : r_li_L{+}L\frac{di_L}{dt}{+}V_0{=}0 \tag{15}$$

$$i_L = C\frac{dv_c}{dt} + \frac{V_o}{R}, \tag{16}$$

where r_l and r_c are the internal resistances of L and C.

Average values of the above equations are expressed as

$$r_l I_L + \left(L\frac{di_L}{dt}\right)_{av} + \frac{1}{T_s}\int_{(d_1+d_2)T_s}^{Ts} V_o dt = V_1 d_1 + V_2 d_2 \tag{17}$$

$$\left(C\frac{dv_c}{dt}\right)_{av} + \frac{V_o}{R} = \frac{1}{T_s}\int_{(d_1+d_2)T_s}^{Ts} i_L dt, \tag{18}$$

where I_L, V_o, $\left(L\frac{di_L}{dt}\right)_{av}$, and $\left(C\frac{dv_c}{dt}\right)_{av}$ are the average values.

At steady state, $\left(L\frac{di_L}{dt}\right)_{av}$ and $\left(C\frac{dv_c}{dt}\right)_{av} = 0$

Therefore, Eqs. (17) and (18) are expressed as

$$r_l I_L + (1-d_1-d_2)V_o = V_1 d_1 + V_2 d_2 \tag{19}$$

$$\frac{V_o}{R} = (1-d_1-d_2)I_L \tag{20}$$

$$\text{Therefore, } I_L = \frac{V_o}{R(1-d_1-d_2)} \tag{21}$$

V_o is obtained by putting Eq. (21) in Eq. (19):

$$V_o = \frac{R(V_1 d_1 + V_2 d_2)(1-d_1-d_2)}{r_l + R(1-d_1-d_2)^2} \tag{22}$$

I_L is obtained by putting Eq. (22) in Eq. (21);

$$I_L = \frac{(V_1 d_1 + V_2 d_2)}{r_l + R(1-d_1-d_2)^2} \tag{23}$$

Expressions of V_o and I_L for ideal MIBBC are obtained by putting $r_l = 0$ in Eqs. (22) and (23), which are similar to Eqs. (3) and (8). For further analysis of the MIBBC, Eqs. (22) and (23) are used.

2.2. System modeling with state space averaging

State space averaging is used for calculating average values of state variables i_L and v_c in steady state [4,22]. State space equations are expressed as follows:

$$\left.\begin{aligned} K\dot{s}(t) &= Ms(t) + Np(t) \\ o(t) &= Cs(t) + Dp(t) \end{aligned}\right\} \tag{24}$$

where the diagonal matrix K contains the values L and C; matrixes M, N, C, and D contain proportionality constant that depends on the operating state of MIBBC; $s(t)$ is the state vector, $p(t)$ is the input vector, and $o(t)$ is the output vector such that

$$s(t) = \begin{bmatrix} i_L \\ v_c \end{bmatrix}, p(t) = \begin{bmatrix} v_1 \\ v_2 \end{bmatrix}, \text{ and } o(t) = \begin{bmatrix} i_1 \\ i_2 \end{bmatrix}$$

State equations for different operating states over single switching cycle are

$$\left.\begin{aligned} K\dot{S}(t) &= M_j s(t) + N_j p(t) \\ o(t) &= C_j s(t) + D_j p(t) \end{aligned}\right\}, \tag{25}$$

where j is the switching state during one switching period.

State equations averaged during time interval t_1, t_2, and t_3 are

$$\left.\begin{aligned} K\dot{S}(t) &= d_1 M_1 s(t) + d_1 N_1 p(t) + d_2 M_2 s(t) + d_2 N_2 p(t) + (1-d_1-d_2) M_3 s(t) + (1-d_1-d_2) N_3 p(t) \\ o(t) &= d_1 C_1 s(t) + d_1 D_1 p(t) + d_2 C_2 s(t) + d_2 D_2 p(t) + (1-d_1-d_2) C_3 s(t) + (1-d_1-d_2) D_3 p(t) \end{aligned}\right\} \tag{26}$$

The system becomes nonlinear due to the presence of time dependent quantities such as duty cycle, voltage, and current in the state equations; thus small-signal AC perturbations are superimposed on time-dependent quantities as follows:

$$\left.\begin{aligned} d_1(t) &= d_1 + \hat{d}_1(t) \\ d_2(t) &= d_2 + \hat{d}_2(t) \\ S(t) &= S + \hat{s}(t) \\ P(t) &= P + \hat{p}(t) \\ O(t) &= O + \hat{o}(t) \end{aligned}\right\} \tag{27}$$

where variables with a cap are small-signal AC perturbations superimposed with DC values. Therefore,

$$\left.\begin{aligned} K\dot{S}(t) &= M_j \hat{s}(t) + N_j \hat{p}(t) + Q_j \hat{d}_1(t) + R_j \hat{d}_2(t) \\ o(t) &= C_j \hat{s}(t) + D_j \hat{p}(t) + E_j \hat{d}_1(t) + H_j \hat{d}_2(t) \end{aligned}\right\} \tag{28}$$

Linearized state space equations of the MIBBC are obtained by putting Eqs. (27) and (28) in Eq. (26). In Eq. (28),

$$\left.\begin{aligned} M_j &= d_1 M_1 + d_2 M_2 + (1-d_1-d_2) M_3 \\ N_j &= d_1 N_1 + d_2 N_2 + (1-d_1-d_2) N_3 \\ C_j &= d_1 C_1 + d_2 C_2 + (1-d_1-d_2) C_3 \\ D_j &= d_1 D_1 + d_2 D_2 + (1-d_1-d_2) D_3 \end{aligned}\right\} \tag{29}$$

Proportionality constants of state space equations are obtained as follows:

$$\left.\begin{aligned} Q_j &= (M_1 - M_3) s + (N_1 - N_3) p \\ R_j &= (M_2 - M_3) s + (N_2 - N_3) p \\ E_j &= (C_1 - C_3) s + (D_1 - D_3) p \\ H_j &= (C_2 - C_3) s + (D_2 - D_3) p \end{aligned}\right\} \tag{30}$$

2.3. Small-signal analysis

From Figures 2a and 2c, the state space equations for time interval t_1, t_2, and t_3 considering nonidealities are expressed as

$$\left.\begin{array}{l}\begin{bmatrix} L & 0 \\ 0 & C \end{bmatrix}\begin{bmatrix} di_L/dt \\ dV_C/dt \end{bmatrix}=\begin{bmatrix} r_l & 0 \\ 0 & -\frac{1}{R+r_c} \end{bmatrix}\begin{bmatrix} i_L(t) \\ v_c(t) \end{bmatrix}+\begin{bmatrix} 1 & 0 \\ 0 & 0 \end{bmatrix}\begin{bmatrix} v_1(t) \\ v_2(t) \end{bmatrix} \\ \begin{bmatrix} i_1(t) \\ i_2(t) \end{bmatrix}=\begin{bmatrix} 1 & 0 \\ 0 & 0 \end{bmatrix}\begin{bmatrix} i_L(t) \\ v_c(t) \end{bmatrix}+\begin{bmatrix} 0 & 0 \\ 0 & 0 \end{bmatrix}\begin{bmatrix} v_1(t) \\ v_2(t) \end{bmatrix}\end{array}\right\} \tag{31}$$

$$\left.\begin{array}{l}\begin{bmatrix} L & 0 \\ 0 & C \end{bmatrix}\begin{bmatrix} di_L/dt \\ dV_C/dt \end{bmatrix}=\begin{bmatrix} r_l & 0 \\ 0 & -\frac{1}{R+r_c} \end{bmatrix}\begin{bmatrix} i_L(t) \\ v_c(t) \end{bmatrix}+\begin{bmatrix} 1 & 0 \\ 0 & 0 \end{bmatrix}\begin{bmatrix} v_1(t) \\ v_2(t) \end{bmatrix} \\ \begin{bmatrix} i_1(t) \\ i_2(t) \end{bmatrix}=\begin{bmatrix} 1 & 0 \\ 0 & 0 \end{bmatrix}\begin{bmatrix} i_L(t) \\ v_c(t) \end{bmatrix}+\begin{bmatrix} 0 & 0 \\ 0 & 0 \end{bmatrix}\begin{bmatrix} v_1(t) \\ v_2(t) \end{bmatrix}\end{array}\right\} \tag{32}$$

$$\left.\begin{array}{l}\begin{bmatrix} L & 0 \\ 0 & C \end{bmatrix}\begin{bmatrix} di_L/dt \\ dV_C/dt \end{bmatrix}=\begin{bmatrix} -\frac{Rr_c+Rr_l+r_cr_l}{R+r_c} & -\frac{R}{R+r_c} \\ \frac{R}{R+r_c} & -\frac{1}{R+r_c} \end{bmatrix}\begin{bmatrix} i_L(t) \\ v_c(t) \end{bmatrix}+\begin{bmatrix} 1 & 0 \\ 0 & 0 \end{bmatrix}\begin{bmatrix} v_1(t) \\ v_2(t) \end{bmatrix} \\ \begin{bmatrix} i_1(t) \\ i_2(t) \end{bmatrix}=\begin{bmatrix} 1 & 0 \\ 0 & 0 \end{bmatrix}\begin{bmatrix} i_L(t) \\ v_c(t) \end{bmatrix}+\begin{bmatrix} 0 & 0 \\ 0 & 0 \end{bmatrix}\begin{bmatrix} v_1(t) \\ v_2(t) \end{bmatrix}\end{array}\right\} \tag{33}$$

From the above state equations, proportionality constants in Eqs. (29) and (30) are determined. By substituting M_j, N_j, C_j, D_j, E_j, H_j, Q_j, and R_j in Eq. (28), small-signal state equations are derived. Therefore,

$$\begin{aligned} L\frac{di_L}{dt} &= V_1d_1(t)+V_2d_2(t)+V_1\hat{d}_1(t)+V_2\hat{d}_2(t)-\frac{Rr_c\,(A)-r_l(B)}{B}i_L(t)-\frac{R\,(A)}{(B)}v_c(t) \\ &\quad+\left\{\left[\frac{Rr_c}{(B)}I_L+\frac{R}{(B)}V_c\right][\hat{d}_1(t)+\hat{d}_2(t)]\right\} \end{aligned} \tag{34}$$

$$C\frac{dv_c}{dt}=\frac{R\,(A)}{(B)}i_L(t)-\frac{1}{(B)}v_c(t)-\left\{\frac{R}{(B)}I_L[\hat{d}_1(t)+\hat{d}_2(t)]\right\} \tag{35}$$

where $A=(1-d_1-d_2)$ and $B=(R+r_c)$

$$I_1=d_1i_L(t)+I_L\hat{d}_1(t) \text{ and } I_2=d_2i_L(t)+I_L\hat{d}_2(t) \tag{36}$$

The mathematical model with load current perturbation (i_o) is developed by taking the Laplace transformation of Eqs. (34) and (35). The open-loop response of the MIBBC is obtained using output current perturbation by

setting $v_1(s), v_2(s), \hat{d}_1(s)$, and $\hat{d}_2$ to zero. Thus,

$$V_c(s) = i_o \times \frac{\left[sL + \frac{Rr_c(A)+r_l(B)}{B}\right]}{s^2LC + s\left[C\frac{Rr_c(A)+r_l(B)}{B} + \frac{L}{B}\right] + \left[\frac{Rr_c(A)+r_l(B)}{B^2} + \left(\frac{R(A)}{B^2}\right)^2\right]} \tag{37}$$

$$\frac{\left[sL + \frac{Rr_c(A)+r_l(B)}{B}\right]}{s^2LC + s\left[C\frac{Rr_c(A)+r_l(B)}{B} + \frac{L}{B}\right] + \left[\frac{Rr_c(A)+r_l(B)}{B^2} + \left(\frac{R(A)}{B^2}\right)^2\right]} = Z_o(s)$$

is the open-loop output impedance of the MIBBC. Therefore,

$$V_c(s) = i_o \times Z_o(s) \tag{38}$$

Similarly, the effect of input voltage perturbation $v_1(s)$ in $v_c(s)$ is derived by

setting $v_2(s)$, $\hat{d}_1(s)$, $\hat{d}_2(s)$, and i_o to zero. Therefore,

$$v_c(s) = \frac{\frac{R(A)}{B}d_1}{s^2LC + s\left[C\frac{Rr_c(A)+r_l(B)}{B} + \frac{L}{B}\right] + \left[\frac{Rr_c(A)+r_l(B)}{B^2} + \left(\frac{R(A)}{B^2}\right)^2\right]} \times v_1(s), \tag{39}$$

where $\frac{\frac{R(A)}{B}d_1}{s^2LC+s\left[C\frac{Rr_c(A)+r_l(B)}{B}+\frac{L}{B}\right]+\left[\frac{Rr_c(A)+r_l(B)}{B^2}+\left(\frac{R(A)}{B^2}\right)^2\right]} = G_{v_1}(s)$ is the transfer function of the MIBBC. Therefore,

$$G_{v_1}(s) = \frac{v_c(s)}{v_1(s)} \tag{40}$$

The effect of $\hat{d}_1(s)$ in $v_c(s)$ is derived by setting $v_1(s)$, $v_2(s)$, $\hat{d}_2(s)$, and i_o to zero:

$$v_c(s) = \frac{(v_1 + \frac{R}{B}v_c + \frac{Rr_c}{B}I_L)\frac{R(A)}{B} - \frac{R}{B}I_L\left(\frac{sL+Rr_c(A)+r_l(B)}{B}\right)}{s^2LC + s\left[C\frac{Rr_c(A)+r_l(B)}{B} + \frac{L}{B}\right] + \left[\frac{Rr_c(A)+r_l(B)}{B^2} + \left(\frac{R(A)}{B^2}\right)^2\right]} \times \hat{d}_1(s) \tag{41}$$

$$G_{vd1}(s) = \frac{v_c(s)}{\hat{d}_1(s)} = \frac{(v_1 + \frac{R}{B}v_c + \frac{Rr_c}{B}I_L)\frac{R(A)}{B} - \frac{R}{B}I_L\left(\frac{sL+Rr_c(A)+r_l(B)}{B}\right)}{s^2LC + s\left[C\frac{Rr_c(A)+r_l(B)}{B} + \frac{L}{B}\right] + \left[\frac{Rr_c(A)+r_l(B)}{B^2} + \left(\frac{R(A)}{B^2}\right)^2\right]} \tag{42}$$

The effect of $\hat{d}_2(s)$ in $v_c(s)$ is derived by setting $v_1(s)$, $v_2(s)$, $\hat{d}_1(s)$, and i_o to zero:

$$G_{vd2}(s) = \frac{v_{c(s)}}{\hat{d}_2(s)} = \frac{(v_2 + \frac{R}{B}v_c + \frac{Rr_c}{B}I_L)\frac{R(A)}{B} - \frac{R}{B}I_L\left(\frac{sL+Rr_c(A)+r_l(B)}{B}\right)}{s^2LC + s\left[C\frac{Rr_c(A)+r_l(B)}{B} + \frac{L}{B}\right] + \left[\frac{Rr_c(A)+r_l(B)}{B^2} + \left(\frac{R(A)}{B^2}\right)^2\right]} \tag{43}$$

Eqs. (42) and (43) are control-to-output transfer functions of the MIBBC.

The impact of perturbation on inductor current is observed by solving Eqs. (34) and (35) for $i_L(s)$ instead of $v_c(s)$. The transfer function $G_{Iv1}(s)$ is obtained by putting the rest of the perturbation to zero. Therefore

$$i_L(s) = \frac{d_1\left(sC+\frac{1}{B}\right)}{s^2LC + s\left[C\frac{Rr_c(A)+r_l(B)}{B}+\frac{L}{B}\right]+\left[\frac{Rr_c(A)+r_l(B)}{B^2}+\left(\frac{R(A)}{B^2}\right)^2\right]}\times v_1(s) \tag{44}$$

For simplification, the term $\frac{d_1\left(sC+\frac{1}{B}\right)}{s^2LC+s\left[C\frac{Rr_c(A)+r_l(B)}{B}+\frac{L}{B}\right]+\left[\frac{Rr_c(A)+r_l(B)}{B^2}+\left(\frac{R(A)}{B^2}\right)^2\right]}$ is considered as $G_{Iv1}(s)$. Therefore, the above equation is simplified as

$$G_{Iv1}(s) = \frac{i_L(s)}{v_1(s)} \tag{45}$$

The above transfer functions are determined with nonidealities considered parasitic of the inductor r_l and capacitor r_c.

Figure 3 shows the frequency response of the transfer functions with nonidealities for the MIBBC parameters given in Table 2, where f_s = switching frequency. These plots are studied and used to design the controllers for the stable operation of MIBBC.

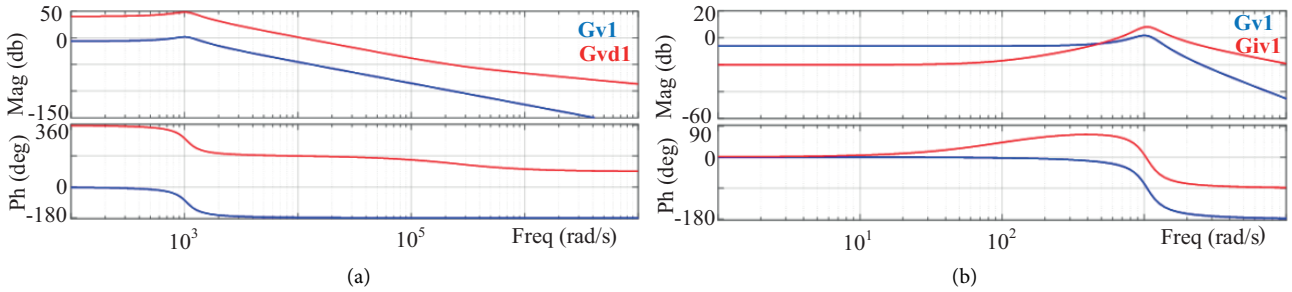

Figure 3. Frequency response of MIBBC. Bode plots of (a) $G_{v1}(s)$ and $G_{vd1}(s)$ (b) $G_{v1}(s)$ and $G_{Iv1}(s)$.

Table 2. MIBBC parameters.

V_1 (V)	V_2 (V)	f_s (kHz)	d_1, d_2	L (μH)	C (μF)	r_l, r_c (Ω)	R (Ω)	V_o (V)
30	18	15	0.25	230	1000	0.05	10	24

3. Control strategy of MIBBC

This section proposes a control strategy for MIBBC. The controllers are designed such that MIBBC operates as per the availability of sources and the load demand. Output voltage is regulated by the appropriate application of gate pulse to the switches, which enhances MIBBC performance. Time multiplexing of gate signals decides the order of operating states in different working conditions. The order of operating states can be changed by appropriate generation of gate pulses. Control of MIBBC is shown in Figure 4. The gate signals of switches S_1 and S_2 are V_{G1} and V_{G2}, respectively. PI controllers are used for voltage and current control.

The load voltage (V_o) is sensed and processed to generate programmed current reference, which is further scaled to get current reference i_{1ref}. The outer voltage loop modifies i_{1ref}, which is based on output voltage error v_e, thereby forcing the load voltage to maintain the desired level as shown in Figure 4a. Thus, the required

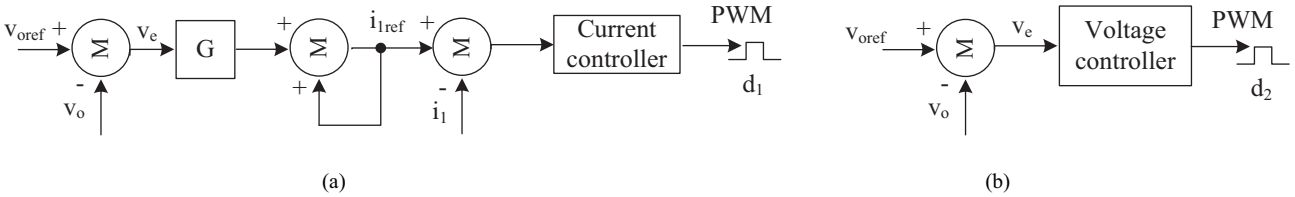

Figure 4. Control of MIBBC (a) generation of V_{G1} (b) generation of V_{G2}.

i_{1ref} is determined for any disturbance in load or input voltage based on the level of v_e. The gain G of the scaling block in the control loop modifies i_{1ref} depending on the level of v_e. Thus, the dynamic response is improved as i_{1ref} is modified in accordance with v_e. The switch current (i_1) is sensed and processed to generate the gate pulses required for switch S_1, which forms a current loop of the MIBBC. The gate pulses required for switch S_2, which forms a voltage loop of the MIBBC, is generated as shown in Figure 4b. Voltage sensor and current sensor are used to sense output voltage (V_o) and switch current (i_1). Thus, the sensed voltage and current are compared with reference voltage and current, and it is then applied to the respective controller.

The PI controllers (compensators) are designed for the MIBBC (plant) using linear control. The MIBBC small-signal control-to-output transfer functions are used to design the controllers. Eq. (42) is a two-pole low-pass filter with a right half plane (RHP) zero introduced by the inductor. It makes the control design for the MIBBC more challenging from the point of view of stability. The RHP zero complicates the problem of stabilizing the control loop. The control-to-output transfer function from Eq. (42) is given as

$$G_{vd1}(s) = \frac{v_{c(s)}}{\hat{d}_{1(s)}} = \frac{26.40 - 107\times10^{-6}s}{230\times10^{-9}s^2+98\times10^{-6}s + 253\times10^{-3}}.$$

The transfer function of a PI controller is expressed as $G_c(s) = \frac{K(1+sT)}{sT}$, where K is the gain and T is the time constant of the PI controller. The PI controller reduces oscillation of the duty cycle during steady state and improves the system's stability. A zero is placed an octave below the cut-off frequency for the current loop PI controller (approximately 250 radians/s). The root locus and bode plot of the current loop PI controller, $G_c(s) = G_{PIi1}(s)$, is shown in Figure 5.

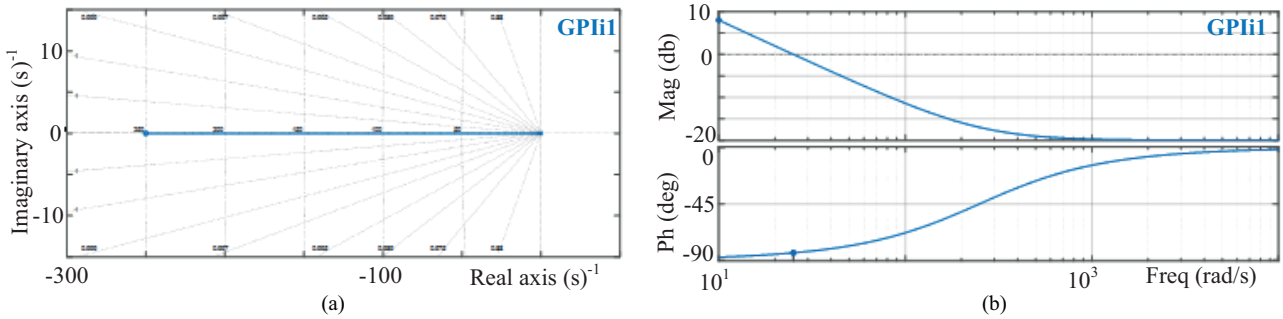

Figure 5. (a) Root locus of $G_{PIi1}(s)$ (b) bode plot of $G_{PIi1}(s)$.

From the bode plot of $G_{PIi1}(s)$, it is observed that the phase margin introduced by the PI controller used for the current loop is 95.7°, thereby making the system stable. The control system is designed to give acceptable performance during the MIBBC operating condition for the following values of K and T of the PI controller:

For voltage loop: $K = 0.1$ and $T = 0.0015$ s; $K_p = 0.1$ and $K_i = 67$.

For current loop: $K = 0.1$ and $T = 0.004$ s; $K_p = 0.1$ and $K_i = 25$.

Here K_p and K_i are proportional and integral gain of the PI controller.

The pulse width modulation (PWM) control technique is used to provide control actions so as to regulate the output voltage of the MIBBC. The function of the controller is to generate switching pulses for the connected sources, which decides the quantity of power supplied by each source. The average value of output current I_o is a function of the average value of input currents I_1 and I_2, i.e. I_o belongs to I_1 and I_2. Hence, the controller decides the supplying source and the quantity of power drawn from it. Therefore, on the basis of load requirement and operating conditions suitable control signals are generated.

3.1. Power sharing and efficiency of the MIBBC

From Eq. (3) it is observed that various combinations of duty cycles d_1 and d_2 can be used to control the load voltage at a desired value when V_1 and V_2 are constant, with different power supplied by each input. The average power supplied by each input is obtained as follows:

$$P_1{=}V_1I_1{=}V_1{\times}d_1I_L \text{ and } P_2{=}V_2I_2{=}V_2{\times}d_2I_L \tag{46}$$

Putting Eq. (23) in Eq. (46) and solving:

$$P_1{=}\frac{(V_1d_1)^2+(V_1d_1{\times}V_2d_2)}{r_l{+}R(1{-}d_1{-}d_2)^2} \text{ and } P_2{=}\frac{(V_2d_2)^2+(V_1d_1{\times}V_2d_2)}{r_l{+}R(1{-}d_1{-}d_2)^2} \tag{47}$$

The total amount of power drawn from the sources is expressed as

$$P_i{=}P_1{+}P_2{=}(V_1d_1{+}V_2d_2){\times}\frac{(V_1d_1{+}V_2d_2)}{r_l{+}R(1{-}d_1{-}d_2)^2} \tag{48}$$

From Eq. (22),

$$P_i{=}\frac{(V_1d_1{+}V_2d_2)V_o}{R(1{-}d_1{-}d_2)} \tag{49}$$

Therefore, power drawn from the connected sources is controlled by appropriate control of the duty ratio.

Output power is expressed as

$$P_o{=}V_o{\times}I_o{=}\frac{V_o^2}{R}{=}\frac{R[(V_1d_1{+}V_2d_2)(1{-}d_1{-}d_2)]^2}{[r_l{+}R(1{-}d_1{-}d_2)^2]^2} \tag{50}$$

Therefore, power efficiency of the MIBBC is expressed as

$$\%\eta = \frac{P_o}{P_i}{\times}100 \tag{51}$$

Power shared by the input sources under various transient conditions of the sources and the load is studied and the performance of the MIBBC is given in Table 3.

Table 3. Performance of the MIBBC during various operating conditions for $V_o = 24$ V.

Sr. No	Case (in steady state $V_1 = 30$ V, $V_2 = 18$ V)	Mode	P_i (W)	P_o (W)	$\%\eta = \frac{P_o}{P_i}$
1	Both V_1 and V_2 are present at $V_1 = 24$ V, $V_2 = 14$ V	V_1 : Boost V_2 : Boost	30.78	28.8	93.57
2	V_1 is acting alone at $V_1 = 30$ V	V_1 : buck	31	28.8	92.9
3	V_2 is acting alone at $V_2 = 18$ V	V_2 : Boost	30.6	28.8	94.12
4	V_1 is cut-off and V_2 has dropped to 8 V	V_2 : Boost	12	10.2	85
5	V_2 is cut-off and V_1 has dropped to 14 V	V_1 : Boost	22.4	19.2	85.71

4. Results and discussion

4.1. Simulation results

To verify the theoretical performance of the MIBBC, simulations are carried out with nonidealities in PSIM software under different steady and transient conditions. Inductor and capacitor design play a vital role, such that the stability and efficiency of the MIBBC is not affected. Eq. (10) is used to obtain the values of L and C. The ON state resistance of MOSFET (R_{DSON}) is 0.036 Ω, forward voltage of diode (V_{DON}) is 1.2 V, and other simulation parameters are given in Table 2.

Solar power is generally used as one of the sources in hybrid power system. The healthy source supplies power to the load if other source is cut off, thereby improving the reliability of the MIBBC. The reliability and power transfer capability are improved by using a solar-battery/UC hybrid system. V_1 is solar source, whereas V_2 is energy storage source (ESS). The power–voltage and current–voltage characteristics of the solar source depend on various parameters such as operating temperature, insolation level, and connected load. The simulation results for CCM operation are analyzed under steady and dynamic conditions. For testing the performance of the MIBBC, different PWM gate signals are applied. Simulation results of gate voltage (V_{G1}, V_{G2}), inductor voltage and current (V_L, i_L), and output voltage and current (V_o, i_o) for various operating conditions with different combination of duty cycles are shown in Figure 6.

The MIBBC operation in boost, buck–boost, and buck mode is shown in Figures 6a–6c, respectively. These waveforms reveal that, irrespective of operating conditions, the output voltage V_o can be regulated at desired value. Figures 6d and 6e show the performance under step decrease and step increase in load, respectively. MIBBC regains the desired value of V_o in a very small interval of time after the transient dies out. The response of MIBBC is satisfactory during steady and dynamic conditions.

4.2. Experimental results

A low-power laboratory prototype was developed for experimental realization of the MIBBC as shown in Figure 7a. Figure 7b shows the solar photovoltaic (PV) panel installed over the laboratory. MOSFETs (IRFP150N; Infineon Technologies, Neubiberg, Germany) and diodes (MUR1560G; ON Semiconductors, Phoenix, AZ, USA) were used as controlling switches in the power circuit. A digital storage oscilloscope (TPS2024B; Tektronix, Beaverton OR, USA), a current probe (A622, Tektronix), and a voltage probe (P5122, Tektronix) were used for measuring current and voltage. A current transducer (LA 25-P; LEM, Geneva, Switzerland) and voltage transducer (LV 20-P, LEM) were used for sensing current and voltage, respectively. The control system for the generation of gate signals at 15 kHz was implemented using a digital signal controller (dsPIC33EP256-MC202; Microchip, Chandler, AZ, USA). L and C were 230 μH and 1000 μF, respectively. Experimental results of

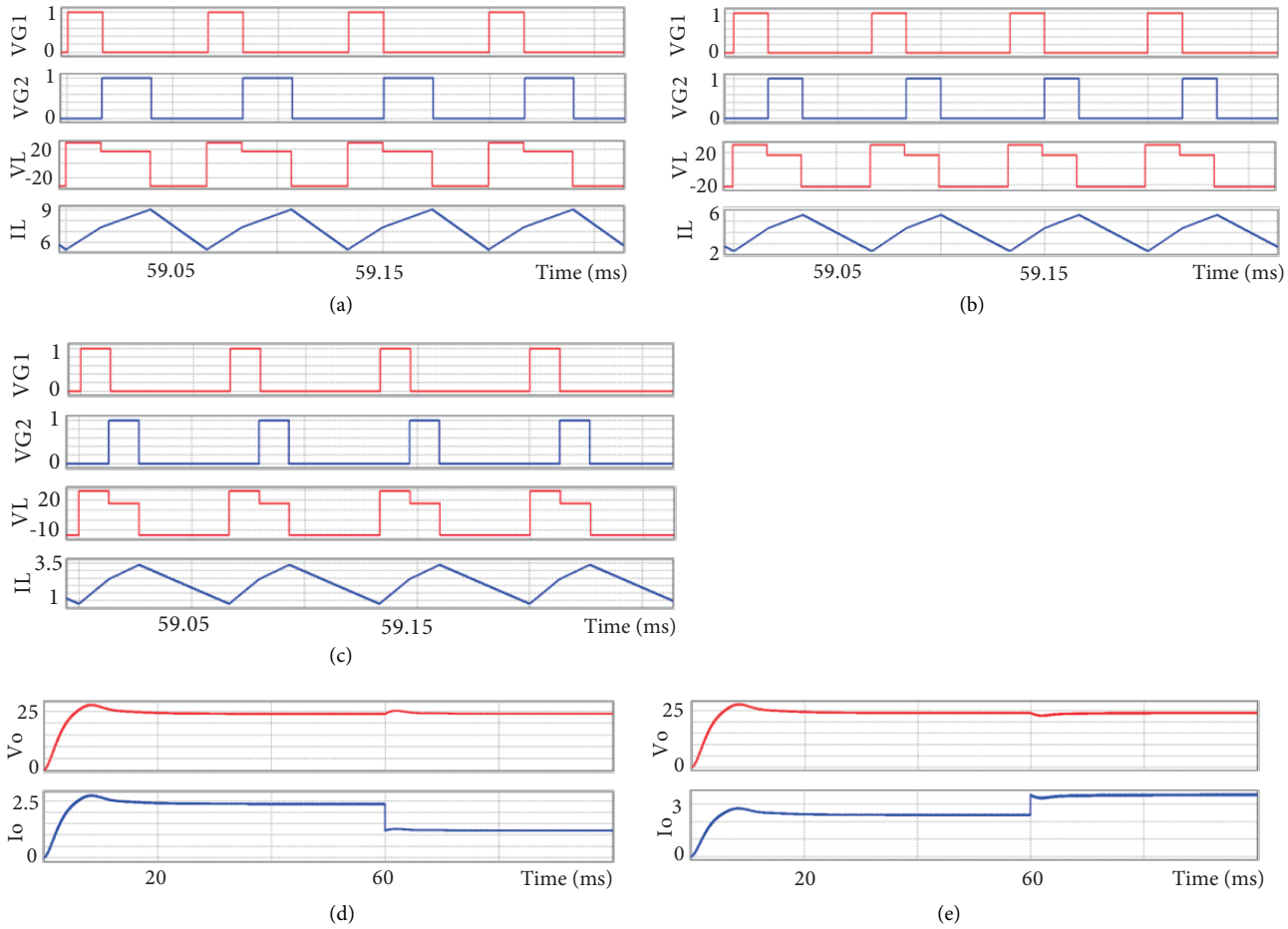

Figure 6. Simulation results of MIBBC (a) gate signal of S_1 and S_2; inductor voltage and current for (b) $d_1 = 0.25$, $d_2 = 0.35$, (c) $d_1 = 0.25$, $d_2 = 0.25$, (d) $d_1 = 0.2$, $d_2 = 0.2$, and (e) output voltage and current for decrease and increase in loading by 50%, respectively.

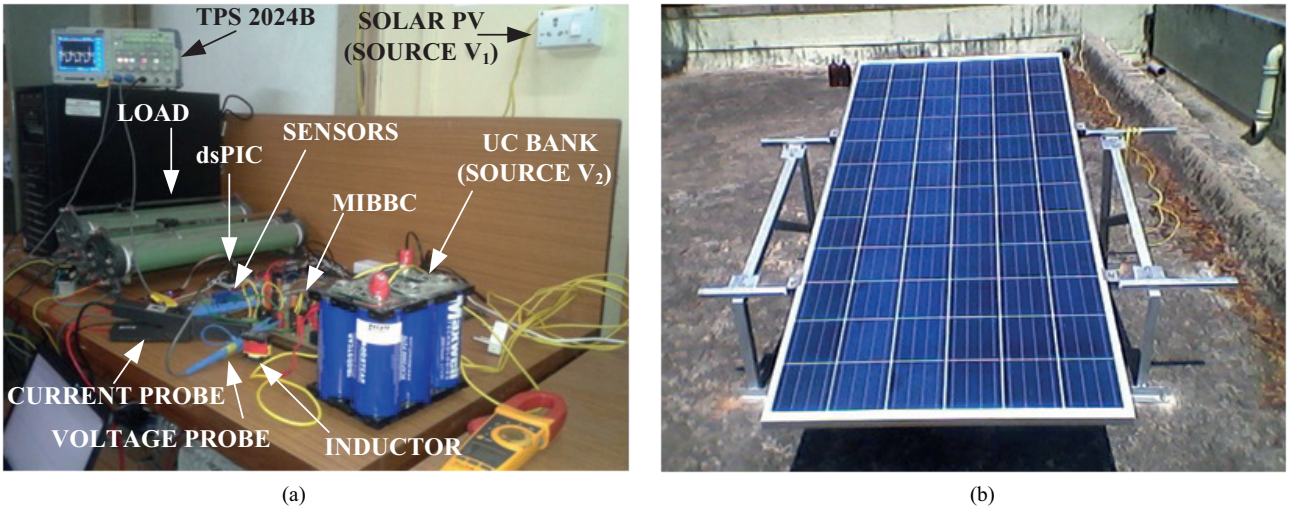

Figure 7. Laboratory set up of (a) MIBBC and (b) solar (PV) panel.

inductor voltage and current (V_L, i_L), output voltage (V_o), and current (i_3) in different modes of operation for various steady and transient conditions are discussed below.

Performance of the MIBBC for different values of V_1 and V_2 to regulate output voltage V_o was studied. The study shows that the MIBBC operates in buck, boost, and buck–boost mode depending on the status of input sources. Figure 8a show waveforms of the MIBBC for V_1 = 24 V, V_2 = 14 V, and V_o = 24 V under steady-state conditions. The current i_3 has two components i_2 and i_L. Rising i_3 indicates charging of L by V_2 in state 2, whereas dropping i_3 shows freewheeling of current i_L in state 3. This proves the operation of MIBBC in states 2 and 3. The inductor charging rate depends on the magnitude of V_1 and V_2, which is clearly observed from i_L waveform. The controller and MIBBC are designed such that V_o is regulated at 24 V for various operating conditions.

Figure 8b shows the reliability of MIBBC operation for output voltage regulation when V_2 is disconnected and V_1 is acting alone at 30 V. This proves the buck mode of operation of the MIBBC. Figure 8c shows the reliability of MIBBC operation for output voltage regulation when V_1 is disconnected and V_2 is acting alone at 18 V. This proves the boost mode of operation of the MIBBC. As seen in Figures 8d and 8e, even though V_2 has dropped to 8 V and V_1 to 14 V, respectively, V_o is regulated. This proves that MIBBC maintains V_o even during variations in source voltages. Variations in source voltage occur due to discharge of ESS or due to change in power supplied by the solar PV module. This proves that input sources having dissimilar current–voltage characteristics such as solar PV, battery, and UCs can be interfaced to the MIBBC.

Transient analysis is performed for step change (increase or decrease) in loading and sudden disconnection of one of the main sources during the operation of the MIBBC, as shown in Figures 8f and 8g, respectively. The MIBBC regains the desired value of output voltage (24 V) in a very small interval of time, after the transient dies out. This is a satisfactory dynamic response of the MIBBC. Thus, output voltage V_o is regulated during various operating conditions. Moreover, there is electrical isolation between input and output throughout the operation of the MIBBC.

The power efficiency of the MIBBC for the given test conditions lies between 85% and 94%. This proves the usefulness of the MIBBC in HESs and RESs. A comparison of the MIBBC with existing work is shown in Table 4. The MIBBC has advantages in most features while it is comparable in the remaining features with respect to number of ports. From Table 4 it is observed that the topology presented in [4] and the proposed work gives isolation without a transformer, but the total number of switches in [4] is more. This is the merit of the proposed work.

5. Conclusion

An MIBBC topology for interfacing dissimilar input sources with flexibility in control is explored for various operating conditions and its performance is studied. Dynamic response of the MIBBC during transients and the ability to handle power during steady state operation is satisfactory. The operation of the MIBBC in buck, boost, and buck–boost mode is verified experimentally. In addition, it has the ability to operate satisfactorily when one of the main sources is disconnected, which leads to improved reliability. The power drawn from both the sources can be controlled by monitoring the source current and the output voltage. Sources and the load are isolated without using a transformer. Battery or UCs are used as an ESS, whereas a solar PV module can be a renewable energy source. The usefulness and feasibility of the MIBBC is verified by performing detailed simulation and experimental studies. Experimental results of the MIBBC prove that it is suitable in hybrid electric applications or renewable energy systems.

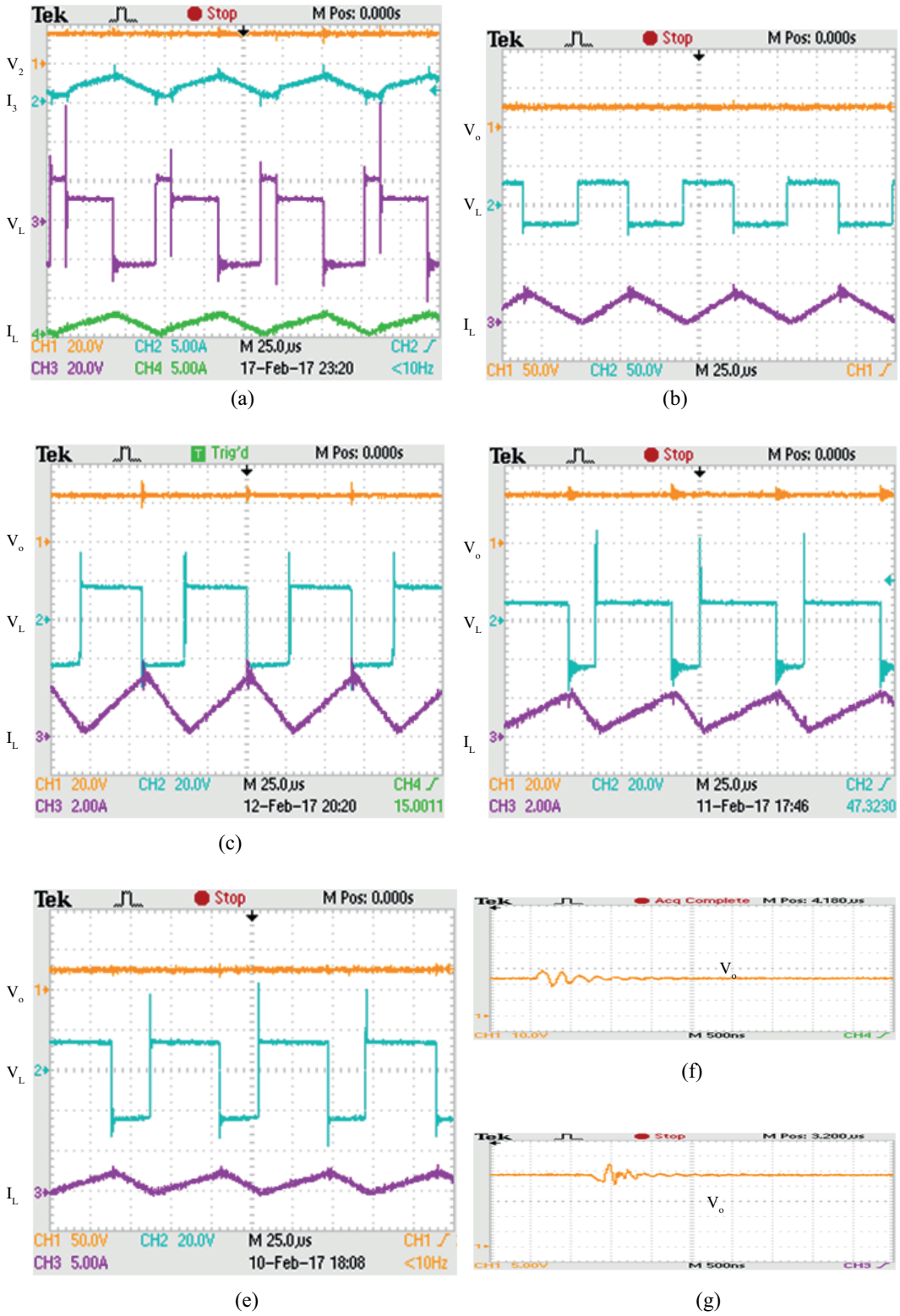

Figure 8. Experimental results of MIBBC for V_o = 24 V when (a) V_1 = 24 V and V_2 = 14 V (b) V_1 is acting alone (c) V_2 is acting alone (d) V_2 has dropped to 8 V (e) V_1 has dropped to 14 V (f) step increase in loading by 25% (g) sudden disconnection of V_1.

Table 4. Comparison of the MICs.

Topology	N_P	N_S	N_D	N_T	N_L	N_C	OM	I	N_W	$\%\eta$
Jiang W [2]	5	8	0	8	4	1	B, b-B	NO	0	80–92
Ahmadi R [3]	3	8	1	9	1	1	b, b-B	NO	0	73–91
Lalit K [4]	3	3	3	6	1	1	b, B, b-B	YES	0	82–91*
Liu F [5]	3	4	2	6	2	2	b	YES	3	88–94
Li W [6]	3	4	4	8	1	2	b-B	YES	$2^{\#}$	87.5–90.9
Dusmez S [7]	3	4	8	12	3	3	B	YES	2	87–88.6
Proposed work	3	2	2	4	1	1	b, B, b-B	YES	0	85–94

N_P: no. of ports, N_S: no. of switches, N_D: no. of diodes, N_T: total no. of switches and diodes, N_L: no. of inductors, N_C: no. of capacitors, OM: operating modes (B: boost, b: buck, $b-B$: buck–boost), I: isolation between sources and load, N_W: no. of transformer windings, $^{\#}$: winding-cross-coupled inductors, $\%\eta$: % efficiency, *: expected % efficiency as mentioned in the literature.

References

[1] Onar O, Khaligh A. A novel integrated magnetic structure based dc/dc converter for hybrid battery/ultracapacitor energy storage systems. IEEE T Smart Grid 2012; 3: 296-307.

[2] Jiang W, Fahimi B. Multiport power electronic interface — concept, modeling, and design. IEEE T Power Electr 2011; 26: 1890-1900.

[3] Ahmadi R, Ferdowsi M. Double-input converters based on h-bridge cells: derivation, small-signal modeling, and power sharing analysis. IEEE T Circuits Syst 2012; 59: 875-888.

[4] Kumar L, Jain S. Multiple-input DC/DC converter topology for hybrid energy system. IET Power Electron 2013; 6: 1483-1501.

[5] Liu F, Wang Z, Mao Y, Ruan X. Asymmetrical half-bridge double-input dc/dc converters adopting pulsating voltage source cells for low power applications. IEEE T Power Electr 2014; 29: 4741-4751.

[6] Li W, Xu C, Luo H, Hu Y, He X, Xia C. Decoupling-controlled triport composited dc/dc converter for multiple energy interface. IEEE T Ind Electron 2015; 62: 4504-4513.

[7] Dusmez S, Li X, Akin B. A new multi input three-level dc/dc converter. IEEE T Power Electr 2016; 31: 1230-1240.

[8] Danyali S, Hosseini S, Gharehpetian G. New extendable single stage multi-input dc–dc/ac boost converter. IEEE T Power Electr 2014; 29: 775-788.

[9] Wai R, Lin C, Liaw J, Chang Y. Newly designed zvs multi-input converter. IEEE T Ind Electron 2011; 58: 555-566.

[10] Yuan Y, Cheng K. Multi-input voltage-summation converter based on switched-capacitor. IET Power Electron 2013; 6: 1909-1916.

[11] Wu H, Zhang J, Xing Y. A family of multi-port buck-boost converters based on dc link inductors (DLIs). IEEE T Power Electr 2015; 30: 735-746.

[12] Nejabatkhah F, Danyali S, Hosseini S, Sabahi M, Niapour S. Modeling and control of a new three-input dc–dc boost converter for hybrid pv/fc/battery power system. IEEE T Power Electr 2012; 27: 2309-2324.

[13] Ouyang Z, Zhang Z, Andersen M, Thomsen OC. Four quadrants integrated transformers for dual-input isolated dc–dc converters. IEEE T Power Electr 2012; 27: 2697-2702.

[14] Wang Q, Zhang J, Ruan X, Jin K. Isolated single primary winding multiple-input converters. IEEE T Power Electr 2011; 26: 3435-3442.

[15] Yang D, Yang M, Ruan X. One-cycle control for double-input dc/dc converter. IEEE T Power Electr 2012; 27: 4646-4655.

[16] Laldin O, Moshirvaziri M, Trescases O. Predictive algorithm for optimizing power flow in hybrid ultracapacitor/battery storage systems for light electric vehicles. IEEE T Power Electr 2013; 28: 3882-3895.

[17] Rahman A, Razak A, Hassan S. A conceptual implementation of a buck converter for an off-grid hybrid system consisting of solar and wind turbine sources. Turk J Elec Eng & Comp Sci 2016; 24: 3782-3791.

[18] Hong J, Lee H, Nam K. Charging method for the secondary battery in dual-inverter drive systems for electric vehicles. IEEE T Power Electr 2015; 30: 909-921.

[19] Wang Y, Liu W, Ma H, Chen L. Resonance analysis and soft switching design of isolated boost converter with coupled inductors for vehicle inverter application. IEEE T Power Electr 2015; 30: 1383-1392.

[20] Chen J, Shen P, Hwang Y. A high efficiency positive buck boost converter with mode-select circuit and feed forward techniques. IEEE T Power Electr 2013; 28: 4240-4247.

[21] Mohan N, Undeland T, Robbins W. Power Electronics: Converters, Applications and Design. 3rd ed. New York, NY, USA: Wiley, 2007.

[22] Kondrath N, Kazimierczuk M. Unified model to derive control-to-output transfer function of peak current-mode-controlled pulse-width modulated DC-DC converters in continuous conduction mode. IET Power Electron 2012; 5: 1706-1713.